Bulletin of the Seismological Society of America, Vol. 104, No. 4, pp. 1650–1662, August 2014, doi: 10.1785/0120130257

Offset of Latest Pleistocene Shoreface Reveals Slip Rate on the Hosgri Strike-Slip Fault, Offshore Central California

by Samuel Y. Johnson, Stephen R. Hartwell, and Peter Dartnell

Abstract The Hosgri fault is the southern part of the regional Hosgri–San Gregorio dextral strike-slip fault system, which extends primarily in the offshore for about 400 km in central California. Between Morro Bay and San Simeon, high-resolution multibeam bathymetry reveals that the eastern strand of the Hosgri fault is crossed by an ~265 m wide slope interpreted as the shoreface of a latest Pleistocene sand spit. This sand spit crossed an embayment and connected a western fault-bounded bedrock peninsula and an eastern bedrock highland, a paleogeography resembling modern coastal geomorphology along the San Andreas fault. Detailed analysis of the relict shoreface with slope profiles and slope maps indicates a lateral slip rate of 2.6 ± 0.9 mm/yr, considered a minimum rate for the Hosgri given the presence of an active western strand. This slip rate indicates that the Hosgri system takes up the largest share of the strike-slip fault budget and is the most active strike-slip fault west of the San Andreas fault in central California. This result further demonstrates the value and potential of high-resolution bathymetry in characterization of active offshore faults.

Online Material: (1) High-resolution bathymetric data for the cross-Hosgri slope and (2) metadata that describes data collection, processing, and formatting.

Introduction

The target of this investigation is the Hosgri fault, one of the major strike-slip faults in the widely distributed transform plate boundary along the west coast of North America (Fig. 1; McCulloch, 1987; Hanson *et al.*, 2004; Lettis *et al.*, 2004; Dickinson *et al.*, 2005; Johnson and Watt, 2012). The San Andreas fault is the primary structure within this boundary, with an estimated slip rate in central California (Carrizo Plain) of ~30–36 mm/yr (Argus and Gordon, 2001; McCaffrey, 2005; Meade and Hager, 2005; Titus *et al.*, 2011). Faults west of the San Andreas fault in central California accommodate a geodetically estimated additional 4–5 mm/yr of dextral slip (Argus and Gordon, 2001; McCaffrey, 2005; Meade and Hager, 2005). The Hosgri–San Gregorio fault system, the most extensive of these western structures, extends about 400 km along the central California coast. At its south end, the Hosgri fault initiates at the northern boundary of the western Transverse Range Province offshore Point Arguello and Point Conception (Steritz and Luyendyk, 1994; Sorlien *et al.*, 1999). As it extends north, this mainly offshore fault system intersects the Big Sur coast at Piedras Blancas and at Point Sur, where strands have been referred to as the San Simeon and Sur faults (Dickinson *et al.*, 2005). Farther north, the fault system extends through the Monterey Bay area as the San Gregorio fault, which continues to the north and merges with the San Andreas fault offshore San Francisco (Bruns *et al.*, 2002; Ryan *et al.*, 2008).

Using high-resolution seismic-reflection and marine magnetic data, Johnson and Watt (2012) showed that the Hosgri fault between Estero Bay and Piedras Blancas is characterized by two distinct strands (Fig. 2). The linear eastern strand is continuous in the offshore for at least 95 km and extends onshore to the northwest at San Simeon. The western strand bends to the northwest and is linked with the Piedras Blancas fold belt, a zone of active contractional deformation that extends beneath Piedras Blancas. Although the western strand coincides closely with the shelfbreak and has locally impressive geomorphic expression (Fig. 2), it can only be traced on the surface and in the shallow subsurface for about 8 km and thus appears to be less important than the regionally continuous eastern strand (Johnson and Watt, 2012).

About 5 km northwest of Estero Point, high-resolution bathymetric data reveal that the eastern strand of the Hosgri fault is crossed by a distinct, linear, southwest-facing bathymetric slope, herein referred to as the cross-Hosgri slope (CHS; Fig. 2). The goal of this investigation is to determine if the CHS is offset by the eastern strand of the Hosgri fault and, if so, to evaluate its use as a piercing point in resolving the rate of lateral fault slip. Such well-constrained slip rates

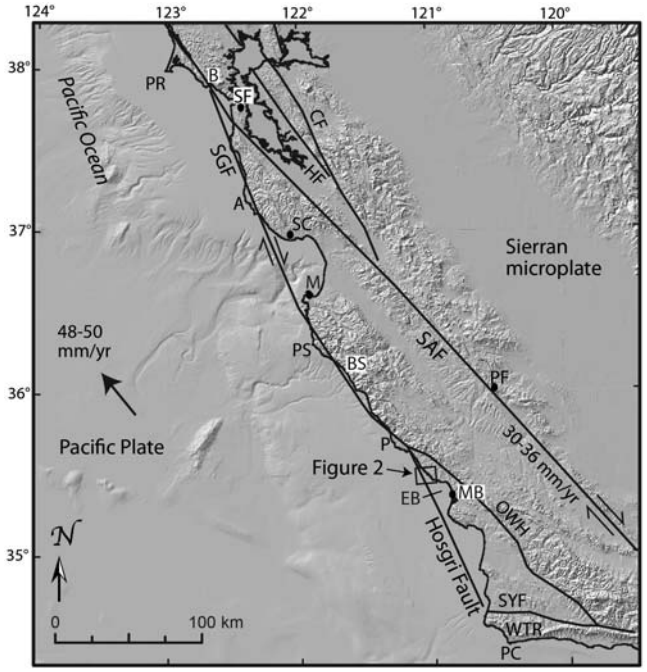

Figure 1. Regional digital elevation model and index map showing significant faults along the central California coast from Point Conception (PC) to Point Reyes (PR). The Hosgri–San Gregorio fault system lies west of and accommodates some of the relative plate motion (48–50 mm/yr) not taken up by the San Andreas fault (30–36 mm/yr). Box shows area of Figure 2. (A, Point Año Nuevo; B, Bolinas; BS, Big Sur; CF, Calaveras fault; EB, Estero Bay; HF, Hayward fault; M, Monterey; MB, Morro Bay; OWH, Oceanic-West Huasna fault; P, Piedras Blancas; PF, Parkfield; PS, Point Sur; SAF, San Andreas fault; SC, Santa Cruz; SGF, San Gregorio fault; SF, San Francisco; SYF, Santa Ynes fault; WTR, western Transverse Ranges.)

are important components of regional earthquake-hazard models and assessments (e.g., Field, 2007; Wills *et al.*, 2008).

Seafloor Mapping

High-resolution bathymetric data in central California were collected by the California State University of Monterey Bay Seafloor Mapping Lab in 2009 and 2010 (see Data and Resources) for the California Seafloor Mapping Program (CSMP), using a combination of sonar systems (400 kHz Reson 7125, 240 kHz Reson 8101, SEA SwathPlus). Most of these data extend from the ~10 m isobath to 5.6 km (3 nautical miles) offshore, the limit of California's State Waters. These data cover more nearshore portions of the Hosgri fault zone (Johnson and Watt, 2012) and provided the first high-resolution imagery of tectonic landforms in the Hosgri fault zone as well as the CHS (Fig. 2). In 2012, the U.S. Geological Survey (USGS) extended high-resolution multibeam coverage beyond State Waters in outer Estero Bay (using a 100 kHz Reson 7111 sonar system) to capture farther offshore portions of the Hosgri fault zone and the unstable shelfbreak to the north (Hartwell *et al.*, 2013). During this cruise, USGS also remapped the small area covering the CHS (Fig. 3), with a survey designed to (1) enhance data density, accomplished by decreasing boat speed and increasing trackline overlap, and (2) minimize poorly oriented data artifacts by following a trackline grid parallel to the slope and subnormal to the Hosgri fault. Such data artifacts are especially problematic given the low relief of this slope (see The Cross-Hosgri Slope section) and hence the need to vertically exaggerate data for analysis and visualization (e.g., Fig. 3). Although we primarily report on and display the USGS dataset in this report (Ⓔ metadata and high-resolution bathymetric data are available in the electronic supplement to this article), we used both the USGS and CSMP data in our slip-rate analyses. Spatial resolution in each dataset is typically 1 m in water depths less than 50 and 2 m for water depths greater than 50 m, and vertical uncertainty is typically in the range of 10–40 cm. The USGS also collected high-resolution seismic-reflection, marine magnetic, and seafloor video imagery databases in this region. These databases include two seismic-reflection profiles (e.g., Fig. 4) and one video transect (e.g., Figs. 3a and 5) that cross the CHS (Sliter *et al.*, 2009; Johnson and Watt, 2012; Golden and Cochrane, 2013).

The Cross-Hosgri Slope

Johnson and Watt (2012) mapped and described the Hosgri fault zone between Point Sal and Piedras Blancas (Fig. 1), designating the part of the zone offshore of Point Estero where the zone bifurcates into eastern and western strands (Fig. 2) as section G. In this area, the eastern strand forms the western margin of a Lazy Z sedimentary basin (Mann, 2007) that pinches out to the north as the fault trace passes through an ~10° transpressive (left) bend. There is a discontinuous, low-relief (< 2 m) scarp along the trace of the eastern Hosgri strand south of the bend; north of the transpressive bend, the eastern strand forms a more prominent scarp (as high as 10 m) along an ~4 km long by ~1 km wide uplift of Tertiary sedimentary rocks, herein referred to as the Hosgri ridge (Fig. 2).

The southeast-trending (~110°) CHS (Figs. 2 and 3) is about 250–280 m wide and 7–9 m high, and extends for about 1700 m across a gap between the south end of the Hosgri ridge and a more gently dipping sediment covered slope on the southwest flank of massive nearshore Cretaceous bedrock outcrops (herein termed the Estero rocks; Fig. 2). This slope dips southwest about 1.6°–2.0°, whereas the seafloor northeast and southwest of the slope dips more gently, approximately 0.4°–0.6°. The water depth at the lower slope break decreases from about 77 to 71 m from northwest to southeast, and the depth of the upper slope break decreases from about 69 to 63 m concurrently. Vertically exaggerated bathymetric imagery (Fig. 3) reveals that the lower slope break ranges from sharp to gradual, whereas the upper slope break is typically sharp and locally embayed.

Figure 4 shows a vertically exaggerated (~8:1) seismic-reflection profile that crosses the entire Hosgri fault zone, with an inset that displays the CHS with more (~12:1) exag-

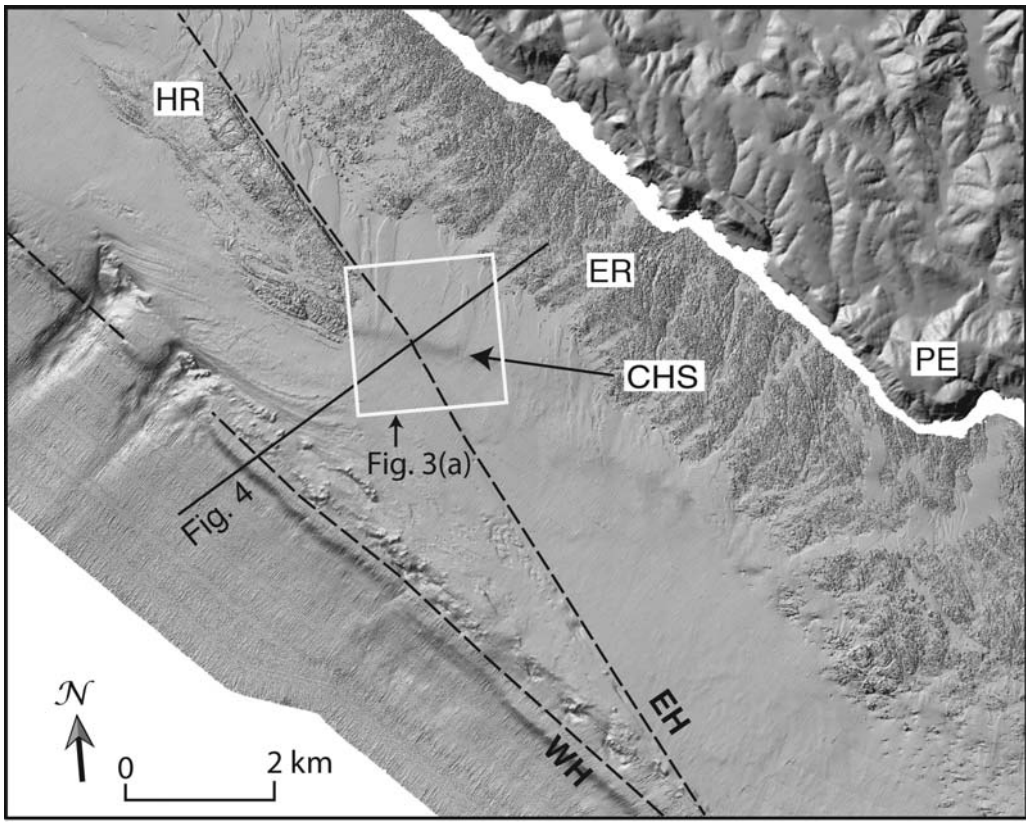

Figure 2. Onshore–offshore hillshade digital elevation model (area shown in Fig. 1) with offshore based on multibeam bathymetry (California State University Monterey Bay Sea Floor Mapping Lab [CSUMB], 2012; Hartwell *et al.*, 2013). Mapping of the eastern (EH) and western (WH) strands of the Hosgri fault zone is based on Johnson and Watt (2012). Note locations of the hillshade image shown in Figure 3 and the seismic-reflection profile shown in Figure 4. (CHS, cross-Hosgri slope; ER, Estero rocks; HR, Hosgri ridge, PE, Point Estero.)

geration. The seismic profile obliquely transects the CHS, which, on this profile, lies above the eastern Hosgri fault strand (Fig. 2). This profile shows that the asymmetric, gently deformed, Quaternary sedimentary basin and the fault zone are overlain by a gently offshore-dipping transgressive surface of erosion (Johnson and Watt, 2012) associated with the sea-level rise following the last glacial maximum (LGM; e.g., Peltier and Fairbanks, 2006; Stanford *et al.*, 2011). The CHS formed on the southwest flank of a sedimentary lens several meters above this transgressive surface of erosion. This post-LGM (latest Pleistocene and Holocene) sedimentary lens thins markedly to the southwest from as much as 16 m to less than 5 m, with most of the thinning coinciding with the CHS (Fig. 4).

The seafloor imagery in Figure 5a and b (locations a and b in Fig. 3a) shows that surface sediment is predominantly bioturbated mud southwest of the CHS at water depths of about 82 and 78 m, respectively. In contrast, the CHS at water depths of about 68 and 70 m (locations c and d in Fig. 3a) is underlain by bioturbated muddy sand with abundant reworked shell debri (Fig. 5c and d). The sediment assemblage on the CHS suggests that a thin veneer of pelagic mud was deposited on top of a substrate comprising sand and shell fragments and that these sediments were subsequently mixed by bioturbation.

Origin and Evolution of the Cross-Hosgri Slope

The CHS is underlain by post-LGM sandy sediments (Figs. 4 and 5), and its origin can be attributed to growth and subsequent submergence of a sand spit and shoreface during the post-LGM sea-level rise. Such sand spits commonly form where the angle of the coast changes direction, such as at a headland (e.g., Dyer and Huntley, 1999). Sediment is deposited in a bar in the lee of the headland as longshore currents expand and dissipate. As the headland bar builds above the surface, littoral drift moves sediment in the direction that the waves are breaking, forming a linear, laterally propagating, subaerial spit and submerged shoreface (occurs between low tide and wave base). Good examples of modern sand spits adjacent to headlands along the high-energy California coast occur at Stinson Beach (Fig. 6) and Bodega Bay; in each case the spits and their shorefaces formed on the southeast side of a coastal headland created by the vertical component of offset on the strike-slip San Andreas fault. This coastal-tectonic geomorphology is similar to the setting we propose below for the CHS, Hosgri ridge, and Hosgri fault.

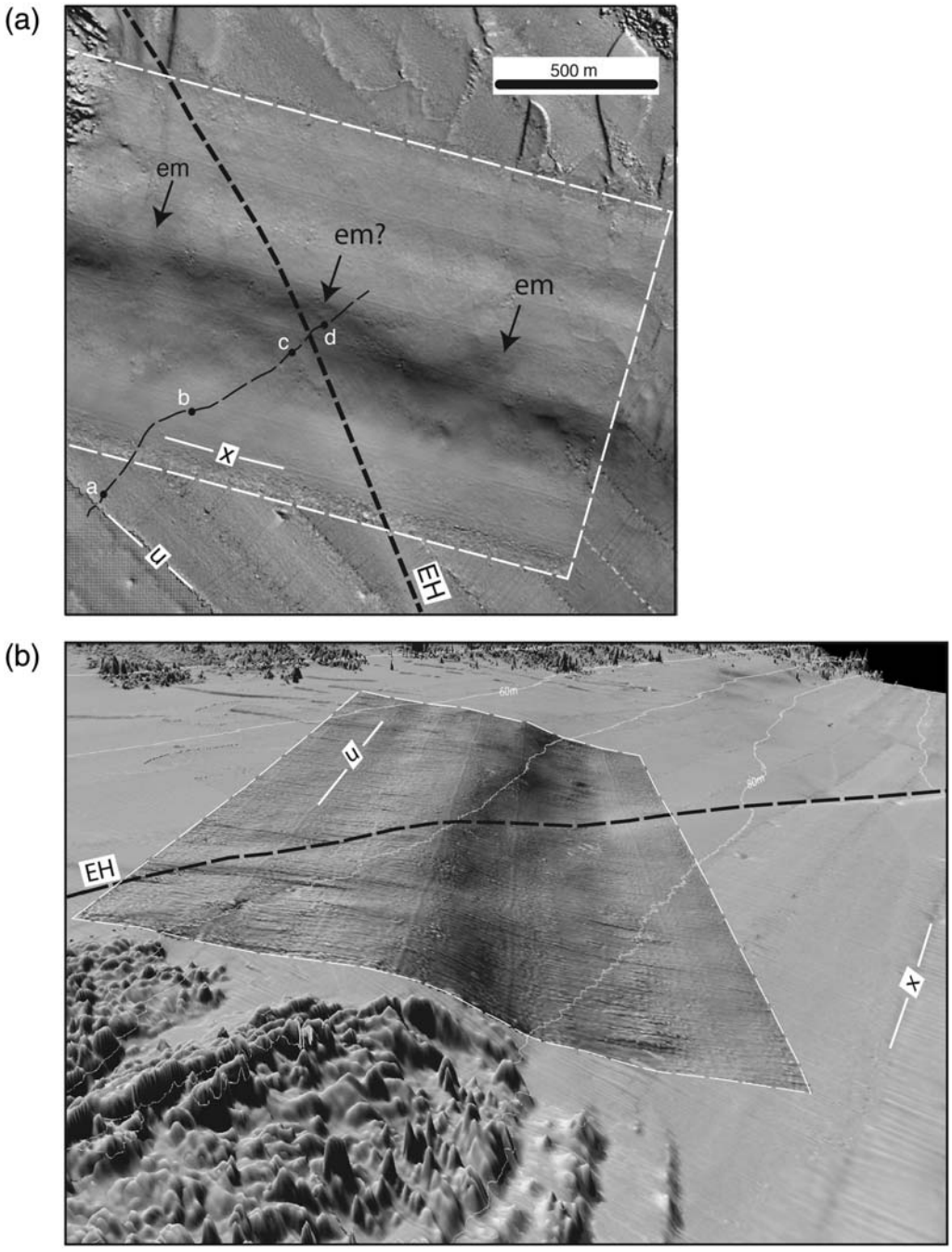

Figure 3. (a) Vertically exaggerated (×20) hillshade digital elevation model of the CHS (area shown in Fig. 2). Dashed white line shows boundaries of U.S. Geological Survey (USGS) multibeam survey, and x and u show trend of trackline artifacts from USGS and California Seafloor Mapping Program (CSMP) surveys, respectively. Curved, northeast-trending, dashed black line shows path of seafloor video camera transect, and a, b, c, and d show locations of seafloor images shown in Figure 5. The heavier northwest trending, dashed black line is trace of eastern Hosgri fault (EH). (b) Vertically exaggerated (×10) perspective view (looking east), showing CHS and trace of the eastern strand of the Hosgri fault.

Our model for the origin and evolution of the CHS is shown in Figure 7, keyed to four different post-LGM sea levels with associated ages based on the global sea-level curves and synthesis of Stanford *et al.* (2011, their fig. 3) who show the LGM at −121 m. These curves are approximations for coastal California, where higher-resolution sea-level curves that include a global isostatic adjustment (e.g., Lambeck and Chappell, 2001) have not been developed, in part due to uncertain and variable vertical land movements associated with active tectonics. However, sea level was probably about −120 m in California during the last lowstand because of the presence of the lowest submerged, post-LGM, wave-cut terrace at this depth adjacent to Hueneme submarine canyon, about 230 km south of the cross-Hosgri slope (Ritchie

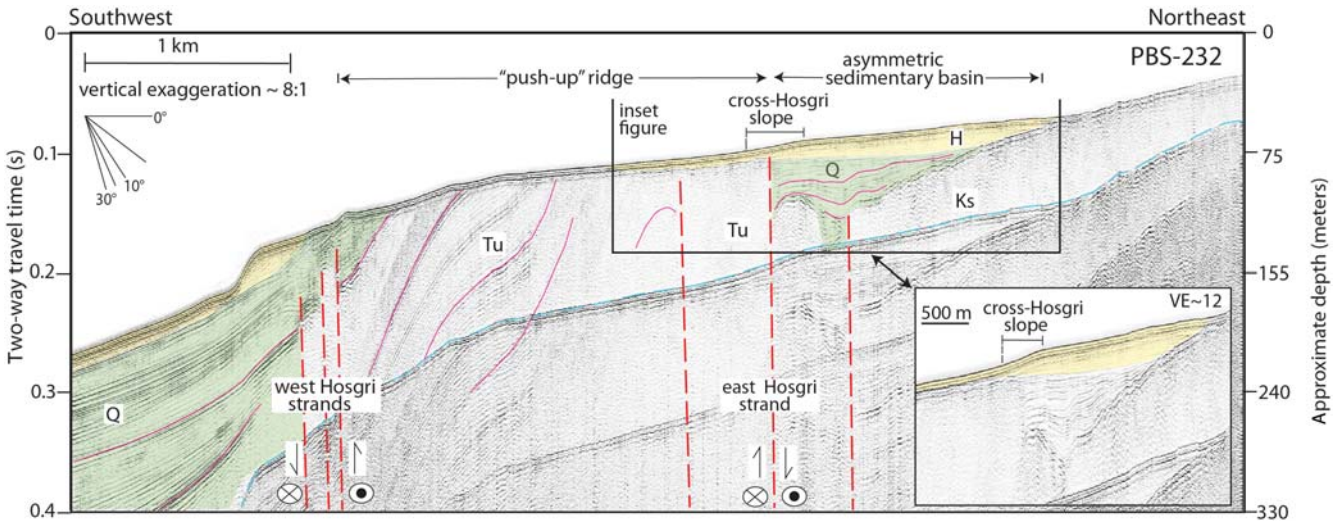

Figure 4. Interpreted USGS seismic-reflection profile PBS-232 crossing the Hosgri fault zone and the CHS (also shown on inset with increased vertical exaggeration [VE]). Location of profile trackline shown in Figure 2. Yellow shading shows latest Pleistocene to Holocene (H) deposits—the base of this unit on the shelf below the CHS is an inferred transgressive surface of erosion; green shading shows inferred late Quaternary (Q) deposits; Tu is inferred Neogene bedrock; and Ks is inferred Cretaceous sedimentary rock. Red dashed lines show faults; thin magenta lines highlight prominent reflections. Blue dashed line shows seafloor multiple (echo of the seafloor reflector). Details of the Hosgri fault are in Johnson and Watt (2012), which shows 20 similar seismic profiles between Point Sal and Piedras Blancas (Fig. 1).

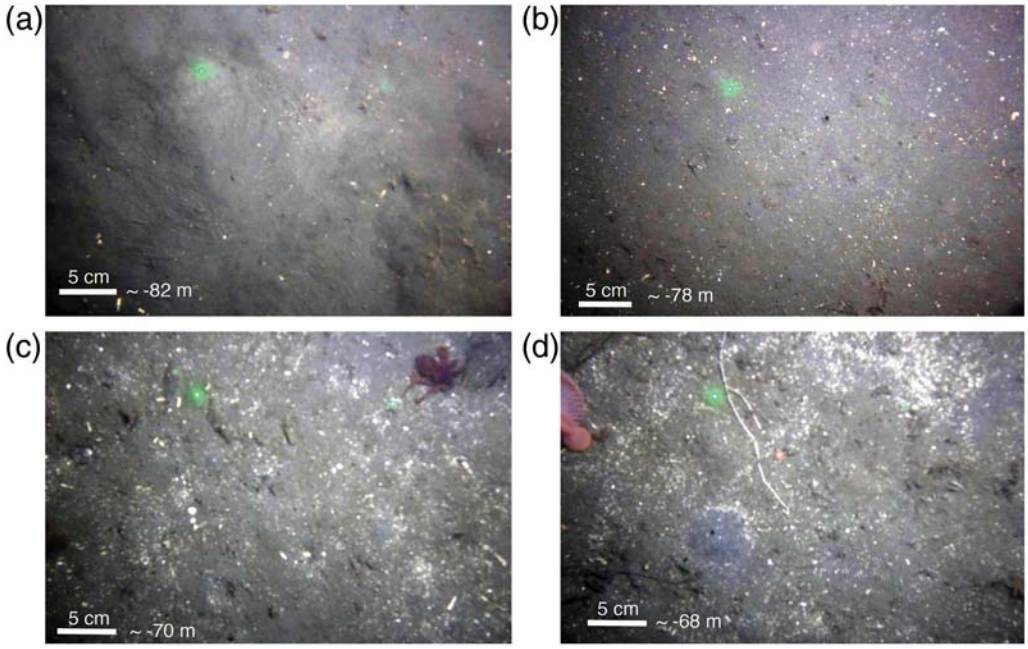

Figure 5. Seafloor imagery of surface sediment at different approximate water depths (e.g., −70 m) and (a, b) southwest of the CHS and (c, d) on the CHS. See text for discussion. Letters correspond to locations in Figure 3a.

and Johnson, 2012). The Stanford *et al.* (2011) model is important because it provides a chronologic framework that will be used (modified slightly, as discussed) in the development of Hosgri fault slip-rate estimates. The key latest Pleistocene to early Holocene time periods for this investigation are the Younger Dryas stadial (~12,800–11,500 yr) and the bracketing meltwater pulse 1a (~14,300–12,800 yr B.P.) and meltwater pulse 1b (~11,500–8800 yr B.P.).

Phase 1, about 13,400 yr B.P. (Fig. 7a)

Sea level was about 80 m below present, and the shoreline was located west of the emergent Hosgri ridge and Estero rocks, as well as the low-lying gap between them where the CHS would soon form. This sea level correlates with meltwater pulse 1a, a period of rapid global sea-level rise (about 10–20 m/1000 yr; Peltier, 2005; Stanford *et al.*, 2011).

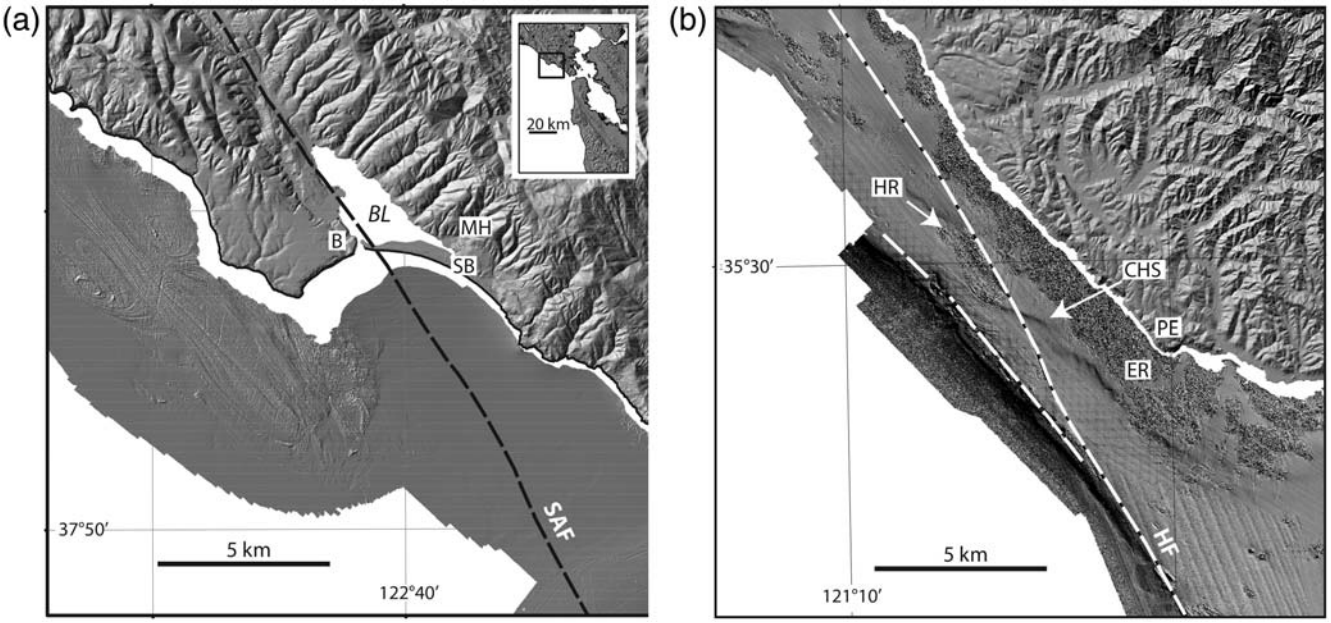

Figure 6. (a) Onshore–offshore hillshade digital elevation model showing the trace of the San Andreas fault (SAF), which cuts through the Stinson Beach (SB) sand spit and Bolinas Lagoon (BL). The sand spit connects the bedrock ridge at Bolinas (B) with bedrock in the Marin Highlands (MH). The shoreface of this sand spit is a modern analog for the CHS. (b) Onshore–offshore hillshade digital elevation model showing the trace of the Hosgri fault (HF) and the Hosgri ridge (HR), cross-Hosgri slope (CHS), and Estero rocks (ER) at the same scale as (a). White areas in the nearshore and offshore on both (a) and (b) lack high-resolution bathymetric data.

Phase 2, about 12,150 yr B.P. (Fig. 7b)

Figure 7b shows sea level about 69 m below present, corresponding to the depth of the upper slope break on the northwest part of the CHS. In this model, a fin-shaped zone between the Hosgri ridge and the Estero rocks was flooded by sea-level rise; this zone was bounded on the south by an ~3 km long, south-facing sand spit and shoreface, which connected the two bedrock uplifts and crosses the Hosgri fault. The trigger for development of the sand spit is inferred to be a significant drop in the rate of sea-level rise associated with the Younger Dryas stadial. Lower rates of sea-level rise allowed a headland bar forming on the southeast flank of the Hosgri ridge to build above sea level and propagate by littoral drift to the southeast as a sand spit. This depth (−69 m) represents the top of the spit's shoreface when the spit was fully developed at the peak of the Younger Dryas, about 12,150 yr B.P. Subaerial parts of the spit are inferred to have been eroded during subsequent rapid sea-level rise (Fig. 7c).

As outlined above, the paleogeography in Figure 7b resembles the setting of the modern Stinson Beach sand spit (Fig. 6), which similarly occurs in a lowland across the trace of a major strike-slip fault, connecting prominent bedrock uplifts to the west and east. Emergent sand dunes on the Stinson Beach spit have reached elevations of as much as 6 m and are highest to the southeast. There are no detailed bathymetric data in shallow water (depths < ~10 m) along the Stinson Beach sand spit, but linear extrapolation from mean high water to the 10 m isobath yields a slope profile similar to that of the CHS, specifically a shoreface no more than 340 m wide, dipping no less than 1.2°–1.4°, and flattening to about 0.2° farther offshore at depths between 10 and 20 m where bathymetric data are available. Shoreface profiles from several locations along the California coast (e.g., work of Barnard *et al.*, 2007, 2009, offshore San Francisco and Ventura) reveal shoreface morphologies (specifically width, height, and dip) that are nearly identical to the CHS.

Phase 3, about 11,700 yr B.P. (Fig. 7c)

Figure 7c shows sea level about 63 m below present, in the latter part of the Younger Dryas stadial. By this time, sediment supply is no longer keeping up with accelerating sea-level rise, and the northwestern part of the paleosand spit has been submerged. With this submergence, the formerly emergent sand spit and upper part of the shoreface along the western part of the paleospit are within wave base (about 8 m) and are being reworked by waves, whereas the lower part of the older shoreface (including the lower slope break of the CHS) has dropped below wave base and is now in a zone of much diminished wave influence and sediment transport. Meanwhile, the eastern part of the sand spit, which may have had higher subaerial relief, is emergent but will be similarly submerged and reworked within a few centuries. This transgressive west-to-east submergence and reworking of the upper part of the CHS is needed to explain the progressive southeastward rise of both the upper and lower slope breaks of the CHS (see The Cross-Hosgri Slope section) and is consistent with simple models for shoreface retreat and vertical

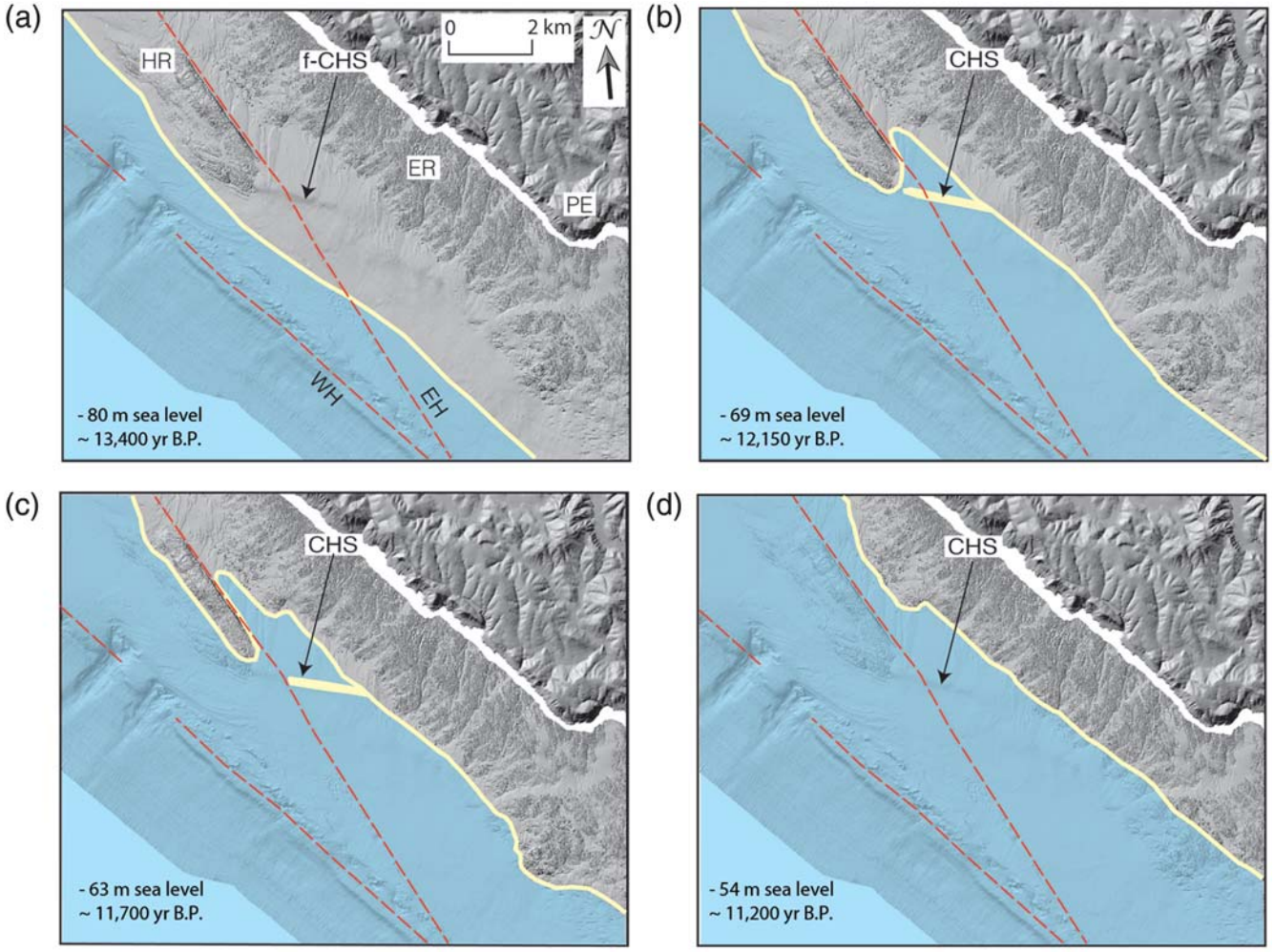

Figure 7. Model for the origin and evolution of the cross-Hosgri slope (CHS) for the area shown in Figure 2, showing progressive sea-level rise following the last glacial maximum in the latest Pleistocene. Faint yellow lines and blue shading shows inferred paleoshorelines and submerged areas, respectively. Dashed red lines show faults. See text for discussion. (EH, eastern strand of the Hosgri fault; ER, Estero rocks; f-CHS, future location of the CHS; HR, Hosgri ridge; PE, Point Estero; WH, western strand of the Hosgri fault.) See text for discussion.

change in response to sea-level rise (e.g., Bruun, 1962; Swift, 1976; Niedoroda *et al.*, 1985).

Phase 4, about 11,200 yr B.P. (Fig. 7d)

Figure 7d shows sea level at about −54 m, during the early phase of meltwater pulse 1b, when rates of sea-level rise grew to about 12–17 m/1000 yr (Stanford *et al.*, 2011). By this time, sediment supply is no longer keeping up with sea-level rise, and the CHS lies below wave base, covered by 10–20 m of water. Reworking and/or reshaping of the CHS is largely over. Minimal downslope sediment transport may continue forced by downwelling currents, gravity, and/or earthquake-induced strong ground motions.

Phase 1–4 Summary, 13,400–11,200 yr B.P. (Fig. 7)

The CHS is thus interpreted as a relict depositional submarine landform. Nearshore sediment accumulated and formed a sand spit and shoreface during a period of reduced sea-level rise during the Younger Dryas stadial. Subsequent rapid sea-level rise during meltwater pulse 1b led to preservation of the submarine shoreface and erosion/beveling of the subaerial sand spit.

The presence of a relict sedimentary landform at this depth along this portion of the California coast is not unique. About 20 km to the north, high-resolution bathymetric data (California State University of Monterey Bay Seafloor Mapping Lab, 2012) show a 3.5 km long, northwest-trending slope at similar water depths, further indication of a significant latest Pleistocene event in which a period of diminished sea-level rise resulted in significant accumulation of coastal sediments. In sequence stratigraphy (e.g., Posamentier, 2002; Catuneanu, 2006, pp. 211–214), similar landforms associated with transgressive systems tracts are referred to as shelf ridges. Preservation of such features results from rapid lateral facies changes during sea-level rise acceleration. In their

discussion of shelf ridges, Dyer and Huntley (1999, p. 1307) note that "it seems that with a fast rise in sea level, moribund forms of all ridge types can be preserved."

Alternative Hypotheses

Despite solid evidence for the submerged sand-spit shoreface origin of the CHS, alternative interpretations were considered. A depositional model in which the CHS formed as a prograding deltaic bar at the mouth of a coastal watershed is considered highly unlikely because onland topographic and shallow bathymetric data do not reveal the presence of a significant coastal watershed in this vicinity. Although the cross-Hosgri trend has a linear trend, a tectonic origin is highly unlikely because (1) mapping based on seismic profiles does not reveal a fault along its mapped trace (about 45° off the trend of the Hosgri fault), and the width (~265 m) and gentle dip (< 2°) of the CHS is not consistent with a fault-scarp origin; and (2) seismic-reflection profiles (e.g., Fig. 4) show that it formed within and above flatlying strata and hence is clearly not a fold scarp that formed above a blind thrust or reverse fault.

What is the Lateral-Slip Rate of the Hosgri Fault?

The lower and upper slope breaks on the CHS each represent potential piercing points for determining the lateral-slip rate of the eastern strand of the Hosgri fault. Given their inferred origin, the lower slope break (the base of the paleoshoreface) should be considerably more reliable because, as sea level rose in the latest Pleistocene, it sank rapidly below wave base and thereafter would have experienced only minimal reworking by storm waves and minor deposition. The upper slope break (the slope break at the top of the paleoshoreface) was submerged at the same rate but started at a higher elevation and occupied a position within wave base (and hence subject to significant wave reworking, deposition, and erosion) for perhaps as much as 1000–2000 years of sea-level rise after it originally formed. Although both the lower slope break and the upper slope break are inferred to be time transgressive from west to east (Fig. 7c and associated discussion), this migration of environments occurred as sea level rose across the entire CHS in about 1000 years or less and, importantly, across the portion of the CHS cut by the Hosgri fault in just a few hundred years.

Visual examination of the vertically exaggerated hillshade image of the CHS (Fig. 3) suggests right-lateral offset on the Hosgri fault. Herein, we use high-resolution multibeam bathymetry (both USGS and CSMP datasets) and derivative slope profiles and slope maps to quantify this offset. We began this effort by plotting a grid of 93 normal-to-slope profiles (Figs. 8a and 9) at a spacing of 12.5 m. We then used these profiles (generally analyzed at half of the vertical exaggeration shown in Fig. 8) to manually locate both lower and upper slope breaks. The lower slope break on slope profiles varies from gradual to sharp (Fig. 9). On some profiles,

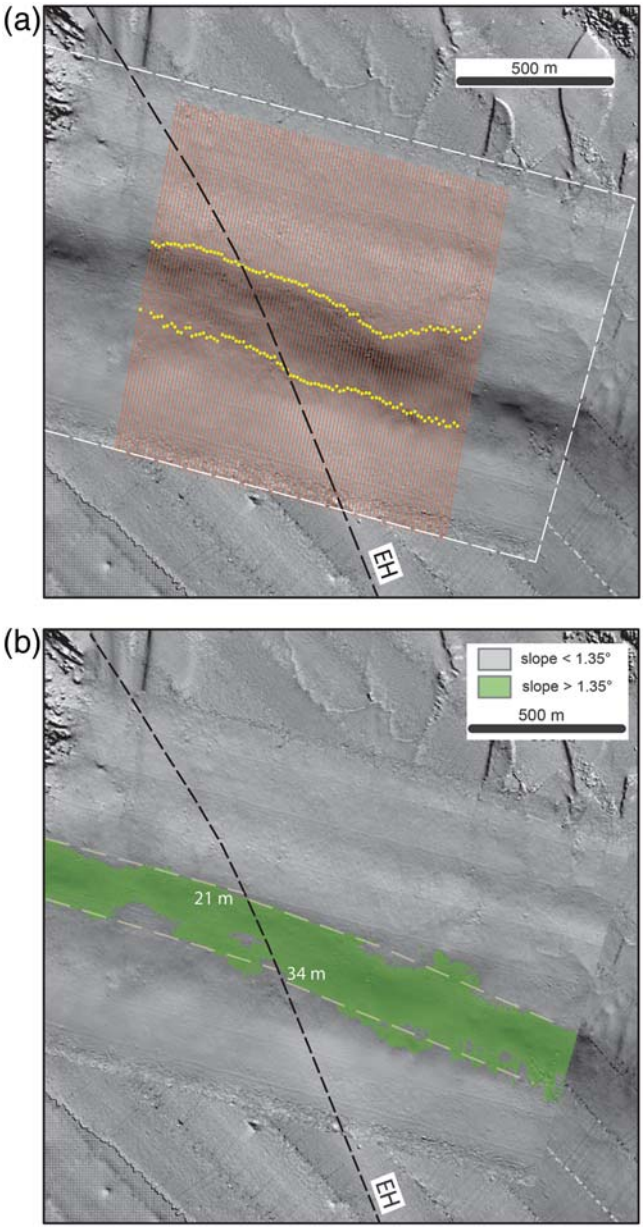

Figure 8. (a) Vertically exaggerated (×20) hillshade digital elevation model (same as in Fig. 3a) of the CHS, with thin red lines showing locations for bathymetric profiles at 12.5 m spacing (see examples in Fig. 9). Yellow dots show locations of lower and upper slope breaks. The dashed white line shows the boundary of the USGS data. (b) Hillshade similar to (a) and Figure 3a, but with green slope overlay and a slope-based interpretation of the lateral offset of the lower and upper slope breaks (dashed yellow lines) that are similar to the offsets determined from slope profiles. (EH, eastern strand of Hosgri fault.) See text for discussion.

the presence of two slope changes near the base of the slope (e.g., Fig. 9a,b) suggests the presence of a thin (generally less than 1 m) sediment wedge; on such profiles, the location of the lower slope break is determined by projecting slope lines through the sediment wedge to an intersection point. The upper slope break on profiles is typically sharp to slightly rounded (Fig. 9). Given issues with small (~1°) slope

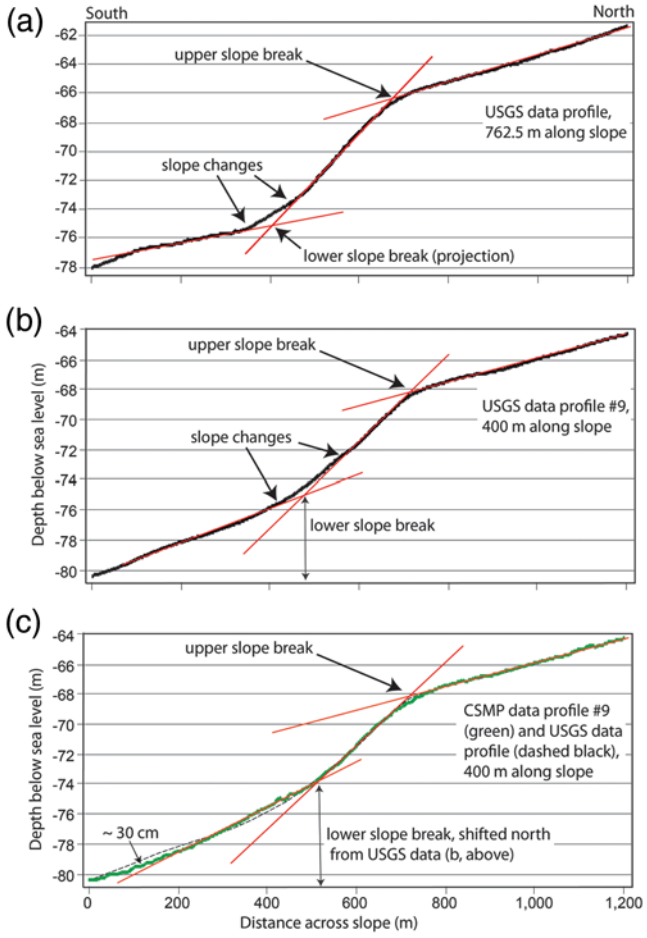

Figure 9. Representative plots of bathymetric profiles (black lines) normal to the CHS (see Fig. 7). Red lines show the slopes used to determine locations of lower and upper slope breaks. Although vertical exaggeration (VE) of these profiles is about 32.5:1, the red slope lines were generally drawn on profiles with VE of 16:1 or less. Note that (b) and (c) compare a profile for the same location generated from the USGS and CSMP multibeam bathymetry data, respectively. See text for discussion.

changes, projections, and rounding, we estimate that uncertainties in locating slope breaks can be as much as 10 m on some profiles. However, the effects of such errors in mapping the slope breaks are minimized by analyzing large numbers of slope profiles at tight profile spacing (Fig. 8a).

The map locations of the upper and lower slope breaks derived from the USGS dataset (Fig. 8a) show that the trends of the locations of the lower slope break both west and east of the Hosgri Fault are relatively linear. The trend of the location of the upper slope break west of the Hosgri fault and within about 250 m of the fault on its east flank have a similar linear trend; farther east, the upper slope break curves around a bulge and embayment, features obvious on the hillshade image of Figure 3a.

The depth of the lower and upper slope breaks are plotted in Figure 10. The obvious ≥70 cm vertical shift in the elevation of the lower slope break (up to the west) precisely locates the Hosgri fault, a position that continues the trend of

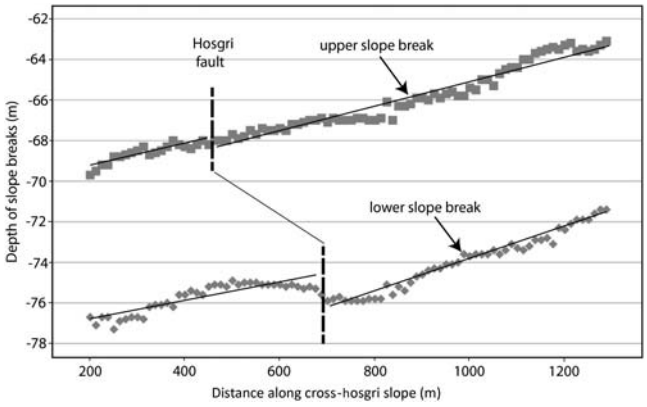

Figure 10. Elevation of the lower and upper slope breaks plotted against distance along the base of the CHS (see Figs. 8 and 9). Linear regression lines (solid black) for points on opposite sides of the Hosgri fault show trends. Vertical exaggeration is 43:1.

the seafloor fault scarp to the south (Fig. 2); north of the CHS, the fault must bend to the northwest about 10° to line up with the prominent fault scarp on the northeast flank of the Hosgri ridge (Fig. 2). Regression lines suggest there may be a much smaller shift (0–30 cm) in the elevation of the upper slope break as it crosses the Hosgri fault, where we locate the fault trace based on apparent lateral offset (e.g., Fig. 11) and slope maps (e.g., Fig. 8b). In addition to helping precisely locate the fault trace, these shifts and regression lines provide an indication of approximate vertical fault offset of the paleoshoreface. The noted ≥70 cm vertical shift of the lower slope break is considered a minimum estimate because the two associated regression lines intersect the projected fault plane 160 cm apart and because the near-fault flattening of slope-break data points west of the fault could reflect frictional drag. Johnson and Watt (2012) have previously documented highly variable vertical slip along the Hosgri fault.

To determine lateral fault offset using the lower slope break as a piercing point, we plotted data points and regression lines obtained from slope profiles located 225 m to the west and 200 m to the east of the fault trace using both the USGS and CSMP bathymetric datasets (Fig. 11). We restricted this analysis to data points within this distance of the fault (1) to acknowledge the time-transgressive origin of the lower slope break (see Fig. 7c and discussion above) and minimize the impact of including data points that represent older or younger phases of dynamic shoreface evolution and (2) to limit the impacts of the depositional or erosional irregularities that occur along the lower slope break farther from the fault.

It is important to note that the lower slope break plots farther north with the CSMP data than with the USGS data. This anomaly reflects a subtle but significant difference in the two datasets, illustrated in the nearly identical slope profiles of the same transect shown in Fig. 9b (USGS data) and 9c (CSMP data). The USGS profile in Fig. 9b (also the black dashed line in Fig. 9c) shows dual slope changes (depths of

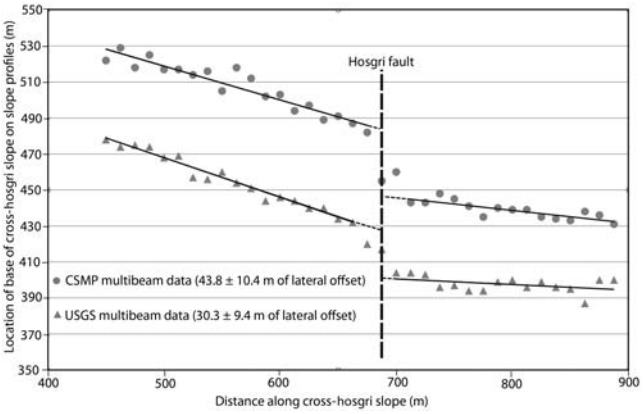

Figure 11. Location of the lower slope break from slope profiles (Figs. 8 and 9) on opposite sides of the Hosgri fault, plotted against distance along the CHS. Graph includes data from slope profiles derived from both USGS and CSMP datasets. Linear regression lines for points on opposite sides of the Hosgri fault show trends, excluding two transitional data points in each dataset along the fault trace. Data reveal approximate lateral offset. Vertical exaggeration is 3.1:1.

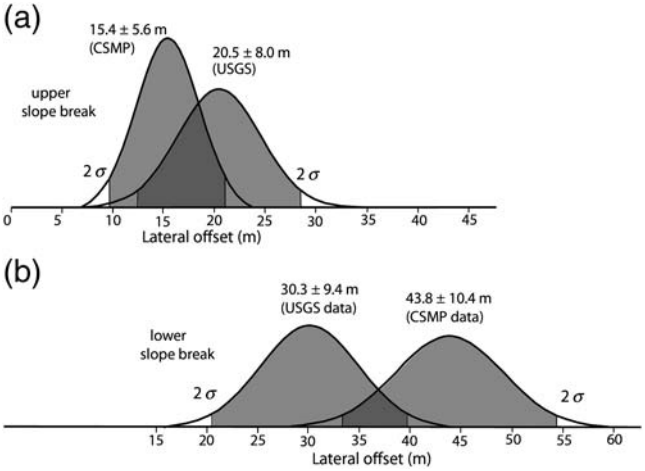

Figure 12. The mean and two standard deviation (shaded areas, 95.45% of area beneath curves) of estimates of lateral fault offset along the (a) upper and (b) lower slope breaks, derived from slope profiles (e.g., Figs. 8 and 9) using both USGS and CSMP multibeam bathymetric data. Note the significant overlap in the distributions for the upper slope break, and the relative lack of overlap in the distributions for the lower slope break. See text for discussion.

72.4 and 75.7 m) at the lower slope break and the presence of a base-of-slope sediment wedge through which slope lines are projected to a depth of 75.2 m. In contrast, the CSMP profile shown in Figure 9c reveals just one slope change at a depth of 73.8 m. This contrast results in a northward shift of 40 m in the location of the lower slope break in the CSMP data compared to the USGS data, despite the fact that at no place do the slope profiles differ vertically by more than 30 cm. This relative northward shift is a consistent feature of the CSMP dataset (Fig. 11).

The two surveys were conducted in different years (CSMP in 2010, USGS in 2012); however, because of the lack of strong currents at such water depths and the absence of significant nearby sediment sources, we think it is unlikely that the contrast in how the two surveys image the lower slope break indicates a temporal seafloor change associated with erosion and/or sedimentation. Instead, we attribute the small but important bathymetry differences to the technological challenges and vagaries involved in repeat mapping of an ~1° slope change in water depths of 70–80 m. There are a large number of variables between the two data-acquisition surveys, including different multibeam sensors with common vertical uncertainties of 10–40 cm, different boats and boat speeds, different trackline orientations and amounts of overlap between tracklines, different sea conditions, and data processing using different water-velocity profiles (collected every few hours in both surveys). Any combination of the above factors could result in the small changes shown in Figure 9b and c and hence the contrasts in the location of the lower slope break determined from slope profiles.

The intersections between regression lines and the Hosgri fault trace for the USGS and CSMP multibeam data indicate 30.3 ± 9.4 m and 43.8 ± 10.4 m of lateral slip (error given as two standard deviations), respectively. Note that the amount of lateral offset exceeds the distance between the regression lines on Figure 10 because the fault cuts obliquely across the slope. The standard deviations for each dataset were determined by constructing a grid parallel to the regression lines for the slope-break location east and west of the Hosgri fault, then differencing each data point west of the fault with each data point east of the fault (285 comparisons). There is minimal statistical overlap between the estimates of lateral slip (Fig. 12) for the two datasets, consistent with the premise that the two surveys imaged the lower slope break differently.

Our paleogeographic reconstruction (Fig. 7 and the preceding discussion) suggests that the lower slope break was submerged and relatively stabilized at about 12,000 ± 500 yr B.P. The analysis based on USGS data therefore suggests a slip rate of 2.6 mm/yr (30.3 m in 12,000 years) with a range (two standard deviations) between 1.7 mm/yr (20.9 m in 12,500 years) and 3.5 mm/yr (39.7 m in 11,500 years). The analysis based on CSMP data suggests a slip rate of 3.7 mm/yr with a range between 2.7 mm/yr (33.6 m in 12,500 years) and 4.7 mm/yr (54.2 m in 11,500 years).

We similarly used slope profiles to locate and plot the upper slope break, focusing on the area 162 m west of and 250 m east of the Hosgri fault trace (Fig. 13). The fault continues its trend from the south, intersecting the upper slope break at a location on the east side of a 50 m wide zone where slope-break locations fall off both the eastern and western trend lines (Fig. 13). Slope profiles derived from the USGS and CSMP surveys are in most cases coincident (e.g., Fig. 8c), thus there are only minimal differences between locations of the upper slope break plotted from the two datasets (Fig. 13). Lateral offsets along the Hosgri fault determined from plots

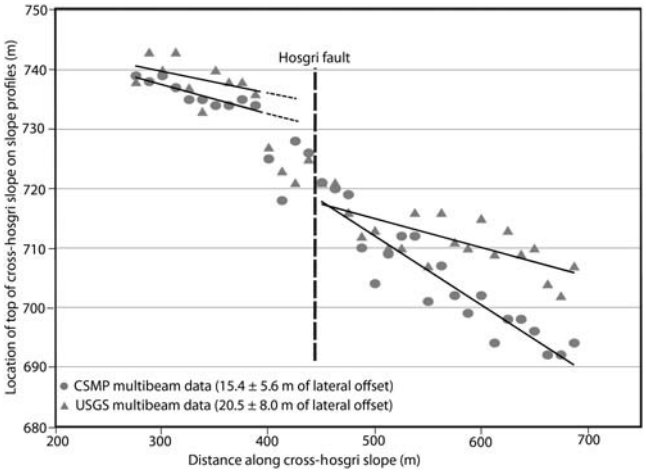

Figure 13. Location of the upper slope break along bathymetric profiles of the CHS (Figs. 8 and 9) on opposite sides of the Hosgri fault, plotted against distance along the CHS. Graph includes data from slope profiles derived from both USGS and CSMP datasets. Linear regression lines for points on opposite sides of the Hosgri fault show trends, excluding four transitional data points in each dataset west of the fault trace. Vertical exaggeration is 5.5:1.

of the upper slope break are 20.5 ± 8.0 m and 15.4 ± 5.6 m for the USGS and CSMP datasets, respectively (again note these amounts exceed the distances between the regression lines on Fig. 13 because the fault cuts obliquely across the slope). These offsets have overlapping distributions (Fig. 12) and yield significantly lower slip rates (~1–2 mm/yr) than those derived from analysis of the lower slope break. However, as described earlier in this section, the upper slope break is considered both a younger and less reliable piercing point. In particular, the presence of a possible erosional embayment along the upper slope break on the east flank of the fault (Fig. 3a) creates an obvious and important level of uncertainty.

Analysis of a suite of slope maps yields a more qualitative assessment of lateral offsets along the Hosgri fault. For example, our best visual placement of the lower and upper slope breaks on the slope map of Figure 8b, generated from USGS data, suggests approximate offsets of about 34 and 21 m for the lower and upper slope breaks, respectively. This simple approach yielded values that lie well within the statistical range of estimates based on slope profiles derived from the USGS data.

Given the above discussion, what is the best estimate for the lateral slip rate of the eastern strand of the Hosgri fault? As described, we consider the lower slope break a much more reliable piercing point, but analysis using two different multibeam surveys yielded two different rates (2.6 ± 0.9 mm/yr and 3.6 ± 1.0 mm/yr) with minimal statistical overlap (Fig. 12). Of these two analyses, we favor the 2.6 ± 0.9 mm/yr rate because (1) it is derived from a multibeam survey specifically designed and conducted (trackline orientation along the slope, increased trackline overlap, and slow boat speeds to increase sounding density) to optimally image the slope-fault crossing and (2) it is more consistent with the smaller offsets suggested by analyses of the younger but less reliable upper slope break. An alternative approach based on the lower slope break yields a combined rate of 3.1 ± 1.5 mm/yr, obtained by weighting the analyses derived from USGS and CSMP datasets equally, averaging the slip rates, and including the full range of statistical uncertainties.

Discussion

Our analysis of the CHS supports a preferred lateral slip rate of 2.6 ± 0.9 mm/yr for the eastern strand of the Hosgri fault. Geodetic syntheses of central California suggest that strike-slip faults in central California west of the San Andreas fault accommodate about 4–5 mm/yr of dextral slip (Argus and Gordon, 2001; McCaffrey, 2005; Meade and Hager, 2005). Results of our work indicate that the Hosgri fault takes up the largest share of this slip budget and is the most active strike-slip fault west of the San Andreas.

Our investigation provides the youngest, most precise, and well-documented rate yet determined for any component of the Hosgri–San Gregorio fault system and is consistent with estimates derived from the closest onland investigations. About 25 km north of the CHS, Hanson and Lettis (1994) and Hall *et al.* (1994) presented onshore geologic data (offset marine terrace strandlines and drainages) from Piedras Blancas (Fig. 1) that suggested the eastern strand of the Hosgri fault has lateral-slip rates of 0.4–11 mm/yr with best estimates in the 1–3 mm/yr range.

Because the recently defined western strand of the Hosgri fault (Johnson and Watt, 2012) is also active, the rate of 2.6 ± 0.9 mm/yr should be considered a minimum for the Hosgri–San Gregorio fault system in this vicinity. The Hosgri slip rate should be higher south of the location where the Hosgri bifurcates into eastern and western strands (Johnson and Watt, 2012), about 8 km south of the CHS (Fig. 2). Indeed, numerous faults converge with or splay off of the Hosgri–San Gregorio fault system (e.g., Lettis *et al.*, 2004; Dickinson *et al.*, 2005; Johnson and Watt, 2012) along its ~400 km length, and it is probable that incremental slip is added or subtracted to the primary fault system at many of these junctures. Further indications of variable slip along the Hosgri–San Gregorio system come from Hanson *et al.* (2004), who suggested that the Hosgri fault loses slip to the south where it converges with the Los Osos fault and several other oblique structures, and Weber (1990), who estimated a slip rate of ~4–10 mm/yr for the San Gregorio fault about 220 km to the north near Point Año Nuevo south of San Francisco (Fig. 1). Thus, the slip rate that we have derived for the part of the fault zone that transects the CHS may not broadly apply to other parts of the Hosgri–San Gregorio fault system. Given this possible variation, there is a clear need for more additional detailed studies of tectonic geomorphology along the system's entire length, with offshore work a priority given the primarily

offshore fault trace. The growing availability of high-resolution bathymetric data will be essential to any future work.

Ryan *et al.* (2012) similarly used high-resolution bathymetry as the key database in determining the slip rate on the San Diego Trough fault zone in the southern California Borderland. Together, that study and our work on the Hosgri fault demonstrate the value of high-resolution bathymetry for fuller characterization of offshore faults. In the same way that high-resolution Light Detection and Ranging (LiDAR) topographic data has contributed to understanding onshore faults and tectonic geomorphology (e.g., Johnson *et al.*, 2004; Arrowsmith and Zielke, 2009), high-resolution bathymetry has the largely unrealized potential to allow rigorous documentation of offshore landforms within active zones of deformation. Analysis of such landforms as strain markers has great promise for determining and/or constraining deformation rates that will have considerable relevance for earthquake-hazard assessment.

Conclusions

The eastern strand of the right-lateral Hosgri fault offshore central California is crossed by an ~265 m wide slope interpreted as the shoreface of a relict, latest Pleistocene sand spit that formed during a period of relatively slower sea-level rise (Younger Dryas stadial) in the latest Pleistocene. This sand spit crossed an embayment, connecting a western fault-bounded bedrock peninsula and an eastern bedrock highland, a paleogeography similar to modern geomorphology along coastal segments of the San Andreas fault. Detailed analysis of the shoreface involving slope profiles and slope maps provides a preferred slip rate of 2.6 ± 0.9 mm/yr. Because the Hosgri locally includes an active western strand, and regionally converges with several other faults, this slip rate should be considered a minimum for the Hosgri fault in central California and should not be applied for the entire ~400 km long Hosgri–San Gregorio fault system. This investigation further demonstrates the importance and potential of high-resolution bathymetry in full hazard characterization of active offshore faults.

Data and Resources

High-resolution bathymetry collected for the California Seafloor Mapping Program (CSMP) is available through the California State University at Monterey Bay Seafloor Mapping Lab at http://seafloor.otterlabs.org/SFMLwebDATA.htm (last accessed April 2014). Ⓔ The U.S. Geological Survey (USGS) high-resolution data over the cross-Hosgri slope (Fig. 3) is available as an electronic supplement to this paper. USGS seafloor video imagery is available through the CSMP Video and Photograph Portal at http://dev.axiomalaska.com/maps/search/usgs.html (last accessed April 2014). USGS seismic-reflection profiles (e.g., Fig. 4) in this area are available in Sliter *et al.* (2009).

Acknowledgments

This work was jointly funded by the U.S. Geological Survey (USGS) Coastal and Marine Geology Program and the Pacific Gas and Electric Company (PG&E) through a Collaborative Research and Development Agreement. We thank David Finlayson, Jenny White, and Pete Dal Ferro for assistance in collection of USGS multibeam bathymetric data. The paper was revised and improved following constructive reviews by Tom Hanks, Yann Klinger, and an anonymous reviewer. We have benefitted from stimulating discussions with Hans AbramsonWard, David Finlayson, Brian Gray, Gary Greene, Phil Hogan, Rikk Kvitek, Stu Nishenko, Gordon Seitz, Steve Thompson, Tom Parsons, and Janet Watt.

References

Argus, D. F., and R. G. Gordon (2001). Present tectonic motion across the Coast Ranges and San Andreas fault system in central California, *Bull. Geol. Soc. Am.* **113,** 1580–1592.

Arrowsmith, J. R., and O. Zielke (2009). Tectonic geomorphology of the San Andreas fault zone from high-resolution topography: An example from the Cholame segment, *Geomorphology* **113,** 70–81.

Barnard, P. L., J. Eshleman, L. Erikson, and D. M. Hanes (2007). Coastal processes study at Ocean Beach, San Francisco, CA: Summary of data collection 2004–2006, *U. S. Geol. Surv. Open-File Rept. 2007-1217*, 171 pp., http://pubs.usgs.gov/of/2007/1217/ (last accessed September 2013).

Barnard, P. L., D. L. Revell, D. Hoover, J. Warrick, J. Brocatus, A. E. Draut, P. Dartnell, E. Elias, N. Mustain, P. E. Hart, and H. F. Ryan (2009). Coastal processes study of Santa Barbara and Ventura Counties, California, *U.S. Geol. Surv. Open-File Rept. 2009-1029*, 926 pp., http://pubs.usgs.gov/of/2009/1029/ (last accessed September 2013).

Bruns, T. R., A. K. Cooper, P. R. Carlson, and D. S. McCulloch (2002). Structure of the submerged San Andreas and San Gregorio fault zones in the Gulf of Farallones as inferred from high-resolution seismic-reflection data, in *Crustal Structure of the Coastal and Marine San Francisco Bay Region, California*, T. Parsons (Editor), *U.S. Geol. Surv. Profess. Paper 1658*, 77–117.

Bruun, P. (1962). Sea level rise as a cause of shore erosion, *J. Waterw. Harbors Div., Am. Soc. Civil Eng. Proc.* **88,** 117–130.

California State University Monterey Bay Sea Floor Mapping Lab (CSUMB) (2012). Seafloor Mapping Lab at CSUMG, http://seafloor.csumb.edu/SFMLwebDATA_c.htm (last accessed April 2014).

Catuneanu, O. (2006). *Principles of Sequence Stratigraphy*, Elsevier, Amsterdam, The Netherlands, 375 pp.

Dickinson, W. R., M. Ducea, L. I. Rosenberg, H. G. Greene, S. A. Graham, J. C. Clark, G. E. Weber, S. Kidder, W. G. Ernst, and E. E. Brabb (2005). Net dextral slip, Neogene San Gregorio–Hosgri fault zone, coastal California: Geologic evidence and tectonic implications, *Spec. Pap. Geol. Soc. Am. Spec. Pap.* **391,** 43 pp.

Dyer, K. R., and C. A. Huntley (1999). The origin, classification, and modeling of sand banks and ridges, *Cont. Shelf Res.* **19,** 1285–1330.

Field, E. H. (2007). A summary of previous working groups on California earthquake probabilities, *Bull. Seismol. Soc. Am.* **97,** 1033–1053.

Golden, N. E., and G. R. Cochrane (2013). California Seafloor Mapping Program video and photograph portal, *U.S. Geol. Surv. Data Set*, http://dev.axiomalaska.com/maps/search/usgs.html (last accessed April 2014).

Hall, N. T., T. D. Hunt, and P. R. Vaughan (1994). Holocene behavior of the San Simeon fault zone, south-central coastal California, in *Seismotectonics of the Central California Coast Ranges*, I. B. Alterman, R. B. McMullen, L. S. Cluff, and D. B. Slemmons (Editors), Geol. Soc. Am. Spec. Pap. 292, Boulder, Colorado, 167–189.

Hanson, K. L., and W. R. Lettis (1994). Estimated Pleistocene slip rate for the San Simeon fault zone, south-central coastal California, in *Seismotectonics of the Central California Coast Ranges*, I. B. Alterman, R. B. McMullen, L. S. Cluff, and D. B. Slemmons (Editors), Geol. Soc. Am. Spec. Pap. 292, Boulder, Colorado, 133–150.

Hanson, K. L., W. R. Lettis, M. K. McLaren, W. U. Savage, and N. T. Hall (2004). Style and rate of Quaternary deformation of the Hosgri fault zone, offshore south-central California, *U.S. Geol. Surv. Bull. 1995-BB*, 33 pp.

Hartwell, S. R., D. P. Finlayson, P. Dartnell, and S. Y. Johnson (2013). Bathymetry and acoustic backscatter, Estero Bay, California, *U.S. Geol. Surv. Open-File Rept. 2013-1225*, http://pubs.usgs.gov/of/2013/1225/abstract.html (last accessed February 2014).

Johnson, S. Y., and J. T. Watt (2012). Influence of fault trend, bends, and convergence on shallow structure and geomorphology of the Hosgri strike-slip fault, offshore central California, *Geosphere* **8,** 25 pp.

Johnson, S. Y., A. R. Nelson, S. F. Personius, R. E. Wells, H. M. Kelsey, B. L. Sherrod, K. Okumura, R. D. Koehler III, R. Witter, L. A. Bradley, and D. J. Harding (2004). Evidence for late Holocene earthquakes on the Utsalady Point fault, northern Puget lowland, Washington, *Bull. Seismol. Soc. Am.* **94,** 2219–2316.

Lambeck, K., and J. Chappell (2001). Sea level change through the last glacial cycle, *Science* **292,** 679–686.

Lettis, W. R., K. L. Hanson, J. R. Unruh, M. K. McLaren, and W. U. Savage (2004). Quaternary tectonic setting of south central coastal California, *U.S. Geol. Surv. Bull. 1995-AA*, 21 pp.

Mann, P. (2007). Global catalogue, classification, and tectonic origin of restraining and releasing bends on active and ancient strike-slip fault systems, in *Tectonics of Strike-Slip Restraining and Releasing Bends*, W. D. Cunningham and P. Mann (Editors), Geol. Soc. Spec. Pub. 290, London, United Kingdom, 13–142.

McCaffrey, R. (2005). Block kinematics of the Pacific–North American plate boundary in the southwestern United States from inversion of GPS, seismological, and geologic data, *J. Geophys. Res.* **110,** 27 pp.

McCulloch, D. S. (1987). Regional geology and hydrocarbon potential of offshore central California, in *Geology and Resource Potential of the Continental Margin of Western North America and Adjacent Oceans: Beaufort Sea to Baja California*, D. W. Scholl, A. Grantz, and J. G. Vedder (Editors), Earth Sci. Ser. 6, Circum-Pacific Council for Energy and Mineral Resources, Houston, Texas, 353–401.

Meade, B. J., and B. H. Hager (2005). Block models of crustal motion in southern California constrained by GPS measurements, *J. Geophys. Res.* **110,** 19 pp.

Niedoroda, A. W., D. J. P. Swift, and T. S. Hopkins (1985). The shoreface, in *Coastal Sedimentary Environments*, R. A. Davis Jr. (Editor), Springer Verlag, New York, New York, 533–624.

Peltier, W. R. (2005). On the hemispheric origins of meltwater pulse 1a, *Quaternary Sci. Rev.* **24,** 1655–1671.

Peltier, W. R., and R. G. Fairbanks (2006). Global glacial ice volume and last glacial maximum duration from an extended Barbados sea level record, *Quaternary Sci. Rev.* **25,** 3322–3337.

Posamentier, H. W. (2002). Ancient shelf ridges–A potentially significant component of the transgressive systems tract–Case study from offshore northwest Java, *Am. Assoc. Petrol. Geol. Bull.* **86,** 75–106.

Ritchie, A. C., and S. Y. Johnson (2012). Detailed geology and geomorphology, Hueneme Canyon, California, sheet 11, in *California State Waters Map Series—Hueneme Canyon and vicinity, California*, S. Y. Johnson, P. Dartnell, G. R. Cochrane, N. E. Golden, E. L. Phillips, A. C. Ritchie, R. G. Kvitek, H. G. Greene, L. M. Krigsman, C. A. Endris, K. B. Clahan, R. W. Sliter, F. L. Wong, M. M. Yoklavich, and W. R. Normark (Editors), *U.S. Geol. Surv. Sci. Invest. Map 3225*, 41 pp., 12 sheets, available at http://pubs.usgs.gov/sim/3225/sim3225_sheet11.pdf (last accessed January 2014).

Ryan, H. F., J. E. Conrad, C. K. Paull, and M. McGann (2012). Slip rate on the San Diego trough fault zone, inner California borderland, and the 1986 Oceanside earthquake swarm revisited, *Bull. Seismol. Soc. Am.* **102,** 2300–2312.

Ryan, H. F., T. Parsons, and R. W. Sliter (2008). Vertical tectonic deformation associated with the San Andreas fault zone offshore of San Francisco, California, *Tectonophysics* **429,** 209–224.

Sliter, R. W., P. J. Triezenberg, P. E. Hart, J. T. Watt, S. Y. Johnson, and D. S. Scheirer (2009). High resolution seismic-reflection and marine magnetic data along the Hosgri fault zone, central California, *U.S. Geol. Surv. Open-File Rept. 2009-1100*, Vol. 1.1, http://pubs.usgs.gov/of/2009/1100/index.html (last accessed March 2013).

Sorlien, C. C., M. J. Kamerling, and D. Mayerson (1999). Block rotation and termination of the Hosgri strike-slip fault, California, from three-dimensional map restoration, *Geology* **27,** 1039–1042.

Stanford, J. D., R. Hemingway, E. J. Rohling, P. G. Challenor, M. Medina-Elizalde, and A. J. Lester (2011). Sea-level probability for the last deglaciation: A statistical analysis of far-field records, *Global Planet. Change* **79,** 193–203.

Steritz, J. W., and B. P. Luyendyk (1994). Hosgri fault zone, offshore Santa Maria basin, in *Seismotectonics of the Central California Coast Ranges*, I. B. Alterman, R. B. McMullen, L. S. Cluff, and D. B. Slemmons (Editors), Geol. Soc. Am. Spec. Pap. 292, Boulder, Colorado, 191–209.

Swift, D. J. P. (1976). Coastal sedimentation, in *Marine Sediment Transport and Environmental Management*, D. J. Stanley and D. J. P. Swift (Editors), John Wiley and Sons, New York, New York, 602 pp.

Titus, S. J., M. Dyson, C. DeMets, B. Tikoff, F. Rolandone, and R. Burgmann (2011). Geologic versus geodetic deformation rates adjacent to the San Andreas fault, central California, *Bull. Geol. Soc. Am.* **123,** 794–820.

Weber, G. E. (1990). Late Pleistocene slip rates on the San Gregorio fault zone at Point Año Nuevo, San Mateo County, California, in *Geology and Tectonics of the Central California Coast Region, San Francisco to Monterey, Volume and Guidebook*, R. E. Garrison, H. G. Greene, K. R. Hicks, G. E. Weber, and T. L. Wright (Editors), Pac. Sec. Am. Assoc. Petrol. Geol., Bakersfield, California, 193–204.

Wills, C. J., R. J. Weldon II, and W. A. Bryant (2008). Appendix A: California fault parameters for the National Seismic Hazard Maps and Working Group on California Earthquake Probabilities 2007, *U.S. Geol. Surv. Open-File Rept. 2007-1437A*, 48 pp.

U.S. Geological Survey
400 Natural Bridges Drive
Santa Cruz, California 95060
sjohnson@usgs.gov

Manuscript received 27 September 2013;
Published Online 1 July 2014